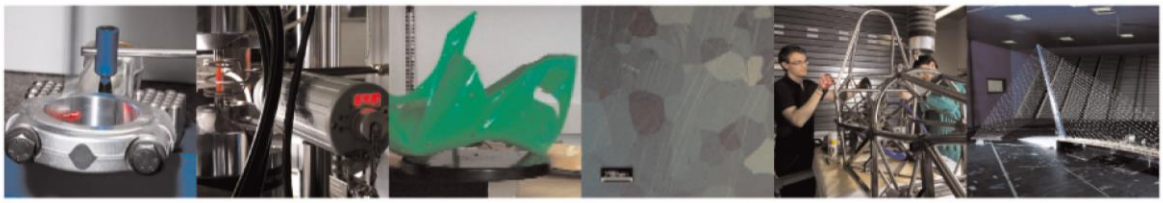

In-situ monitoring of image texturing via random forests and clustering with applications to additive manufacturing

Caltanissetta, Fabio; Bertoli, Luisa; Colosimo, Bianca Maria

This is an Accepted Manuscript of an article published by Taylor & Francis in IISE Transactions on 11 Sep 2023, available online:
http://www.tandfonline.com/10.1080/24725854.2023.2257255.

In-situ Monitoring of Image Texturing via Random Forests and Clustering with applications to Additive Manufacturing

Fabio Caltanissetta, Luisa Bertoli, Bianca Maria Colosimo*

Dipartimento di Meccanica, Politecnico di Milano, Via La Masa 1, 20156, Milan, Italy

* Corresponding author: biancamaria.colosimo@polimi.it

Abstract

The attention toward in-situ monitoring in Additive Manufacturing (AM) has significantly increased over the last years, paving the way to a paradigm shift for quality monitoring and control via big data analysis of signals, images, and videos. In-situ quality monitoring represents an opportunity for waste reduction and first-time-right production via inline detection of process flaws, which allows early identification of scraps and the possibility of correcting actions for first-time-right production. This paper presents a solution for in-situ monitoring of images taken layerwise in material extrusion AM. Compared with the existing solutions, mainly focusing on monitoring the shape deviation observed at each layer with respect to the nominal shape, this paper focuses on monitoring the internal surface texture with the aim of detecting over- and under-extrusion flaws. Inspired by an approach developed by Bui and Apley for textile image monitoring, we propose a solution for in-situ monitoring of textured surfaces which is based on combining Random Forests with clustering to automatically identify defective locations layerwise. A real case study based on Fused Filament Fabrication is used to compare the performance of the novel proposed solution with the original one and identify an appropriate direction for future research.

Keywords: statistical quality monitoring, in-situ monitoring, image, Random forests, clustering, additive manufacturing

1. Introduction

In the last decades, Additive Manufacturing (AM) technologies have attracted increasing interest in many industrial sectors for producing highly functionalized, complex, and customized parts (Holmes,

2019; Qin *et al.*, 2019). Among the AM technologies, Material Extrusion (ME) processes are experiencing significant growth for their huge flexibility, which makes the technology suitable at many different scales (from big area AM to microfabrication) for many different materials (techno-polymers and composites, hydrogels, metals) in many industrial sectors (aerospace, tooling and molding, oil and gas, energy and biomedical sectors). These technologies entail layerwise deposition of the material through a nozzle, which is commonly moved by a gantry system in the x and y directions. When a layer is entirely completed, the distance between the last layer and the nozzle tip is increased along the z-axis of a fixed quantity, i.e., the layer height. This process is iterated until all the layers are deposited.

Regardless of the big potential, the occurrence of a wide range of part defects, which may arise in different scales and frequencies, still represents one of the major barriers to the technology breakthrough. However, the recent advances in sensing technologies (images and video-imaging) combined with novel solutions for big and complex data mining for quality monitoring and control triggered the use of in-situ solutions for zero-defect manufacturing (Colosimo *et al.*, 2018a; Colosimo 2018). In situ monitoring consists of acquiring all the relevant information on the process behavior and part quality during the printing process to detect or even anticipate process instability and flaws.

In this framework, an increasing number of studies (Fu et al., 2020, Oleff et al., 2019) focus on the analysis of pictures taken layerwise at the end of the deposition phase. All these studies can be classified in two main research groups, depending on their target objective.

Approaches in the first stream focus on detecting dimensional and geometrical errors by comparing the geometry of the last layer deposited with the nominal geometry (Nuchitprasitchai *et al.*, 2017a and 2017b; He *et al.*, 2019; and Straub, 2015), similar to what is done for Powder Bed Fusion AM processes (Caltanissetta *et al*., 2018; Pagani *et al*., 2020; Colosimo *et al*., 2022). In this class, some recent approaches suggested using Artificial Intelligence and Machine Learning for monitoring purposes, as in the case of Narayanan *et al.*, (2019), who compared Support Vector Machine and Convolutional Neural network to detect images with geometrical defects showing a classification accuracy of 98.2% and 99.5%, respectively. Similarly, He *et al.*, (2018) presented a control charting solution for monitoring the maximum deviation of the printed layer from the reference contour. Wu *et al.*, (2017), compared a naïve

Bayes classifier and a regression tree to classify infill images in defective and non-defective layers, reaching an accuracy of around 85% and 95%, respectively.

The second research stream focused on the analysis of the top layer texture to detect local anomalies in the pattern as a symptom of deposition errors. These anomalies usually called under and over-extrusion, are responsible for a large variety of final part defects, such as inter-bead and inter-layer porosity, undesired surface texture, and poor material bonding. These issues are particularly detrimental to the final part integrity, and they are difficult to identify and recover through post-processing operations.

Okarma and Fastowicz studied anomalies in ME, defining some possible statistics for processing images for extrusion processes (Okarma *et al.*, 2016; Okarma *et al.*, 2019; Fastowicz *et al.*, 2019; Okarma and Fastowicz 2020). This stream of research follows the main idea of monitor surface texture by controlling the stability of some synthetic indexes representing the surface pattern (Sun *et al*., 2017), possibly after surface pre-processing (as segmentation in Alqahtani *et al*., 2020).

Different authors then suggested supervised learning solutions to classify defects in printed jobs (Liu *et al.*, 2019; Jin *et al.*, 2019; Banadaki *et al.*, 2020; Wang *et al.*, 2020). With reference to ME, a quite different approach was recently proposed in the literature to monitor the process dynamic via statistical quality monitoring of thermal video-imaging for hot- and cold-spots detection (Caltanissetta *et al*., 2022).

Supervised approaches require both in-control (IC) and out-of-control images (OOC) and this is why all these methods are usually problem-dependent, as prior knowledge of the specific flaws is needed for method design. As top-surface flaws can occur in different sizes, shapes, and severity, and all these possible conditions are usually not known in advance. Moreover, the printed material, the process parameters, the material color, and the environmental illumination usually cause over-variability and this is why supervised solutions can be hardly exported to work in different settings.

In this paper, we aim to develop an unsupervised solution for statistical quality monitoring of additively manufactured surfaces where texture and topology defects are of interest. To this aim, we will assume that only a short set of in-control frames need to be known in advance to design the approach (Phase 1 or design phase) and then make it able to detect any unnatural departure from the in-control state.

The proposed solution is inspired by a methodology recently proposed by Bui and Apley (2018) (B&A) for statistical quality monitoring of textile patterns, which is more generally suitable for stochastic textured surfaces, i.e., surfaces where no "gold standard" shape can be clearly identified as a quality feature of interest, as the ones shown in Figure 1.

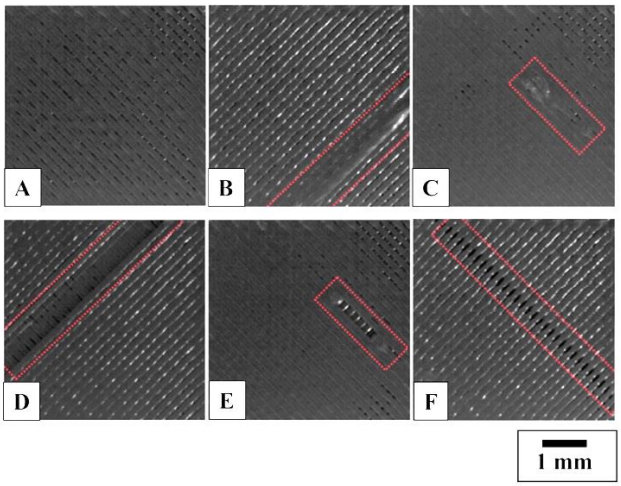

Figure 1- Examples of in-situ images with (a) absence of defects (b) over-extrusion in an entire bead (c) over-extrusion in a portion of the bead (d) under-extrusion in multiple consecutive beaI(e) under-extrusion in a portion of the bead (f) inter-bead porosity.

Starting from the original approach by B&A, our proposed method introduces several new features to improve the effectiveness and robustness of the quality monitoring solution when layerwise images of textured surfaces obtained via ME are considered. As images obtained in this AM context present several elements in common with other stochastic textured images (e.g., images in milling, welding, shot peening, and rolling), we do believe that our newly proposed solution can be effective in many other manufacturing applications.

In particular, the three main novelty elements proposed in our method consist of: i) a different windowing strategy in the modeling step; ii) the use of Random Forests instead of Regression Trees in the texture modeling stage; iii) a novel algorithm based on k-mean clustering for out-of-control detection. All these advantages derived from these novelty elements are discussed and analyzed with respect to a real case study where 188 layers observed on two different builds were monitored. Our

approach is based on learning one single image of the in-control state and then moving to Phase 2 of control charting for all the new layers. Starting from the preliminary results presented in Bertoli *et al*. (2021), this paper explores and discusses all the advantages of the newly proposed solution for surface texture monitoring in 3D printing. In particular, the manuscript analyses the effect of the surface texture orientation, the selection of moving window dimensions in model training and compare our newly proposed methodology with state-of-the-art competitors currently used for layerwise image monitoring in ME. In order to show the flexibility of our newly proposed solution, application to lattice- or grid-textured 3D printed surfaces is also presented.

The paper is organized as follows. Section 2 describes the case study. Section 3 discusses the original B&A and the newly proposed methodologies. Section 4 presents the application of the proposed solution on a real case study. Section 5 shows the performance comparison and Section 6 presents an extension of the approach to a lattice- or grid-like textured surfaces. Eventually, the conclusions are presented in Section 6.

3. Anomaly detection on Stochastic Textured Surface

3.1 The B&A approach

The approach proposed by Bui and Apley is summarized in Figure 2, where it is shown that the method is based on three main steps, that will be described in the following.

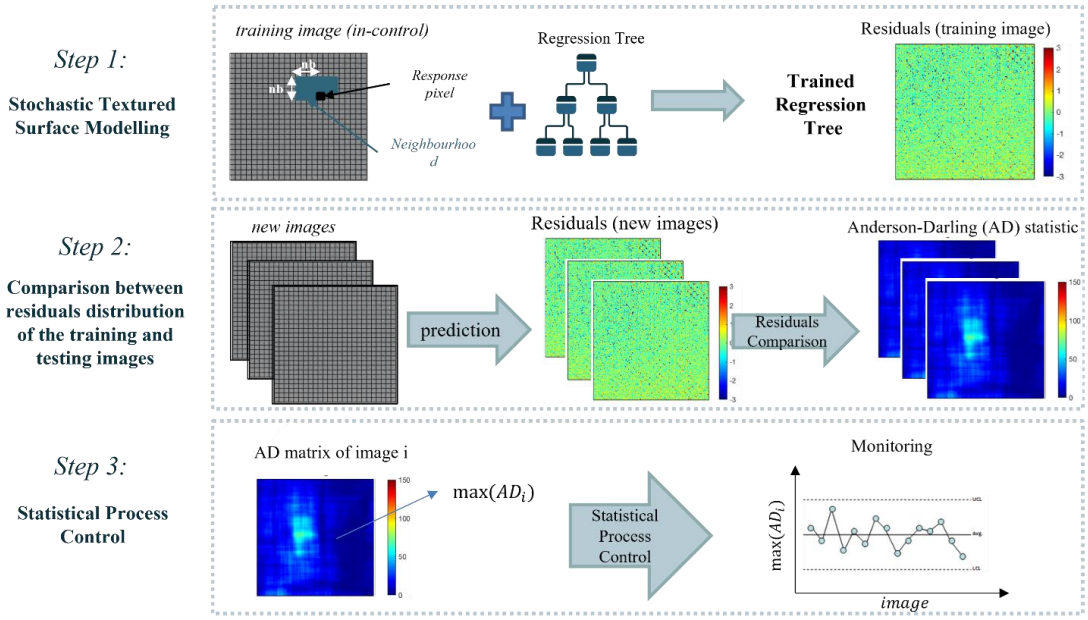

Figure 2 Schematic representation of the B&A algorithm

At the first step, a modeling step is carried out starting from a set of stochastic textured images $\boldsymbol{I}_j$ (j=1,2,…,N), where each image is composed by *M* pixels whose intensities are stored in the vector $\boldsymbol{Y}_j = [y_{j,1}, y_{j,2}, \dots, y_{j,M}]^{\boldsymbol{T}}$. Following B&A, all the pixels in $\boldsymbol{Y}_j$ are listed considering a row raster scan pixel sequence from the left to the right, and then moving from the top to the bottom image rows. For the sake of simplicity, the index *j* is omitted from now on, since we refer to a single generic image *j*. According to B&A, the joint distribution $f(\boldsymbol{Y})$ provides the complete description of the statistical behavior of the grayscale intensity in the image, but its calculation is computationally intractable. For this reason, the authors suggest considering the factorization of $f(\boldsymbol{Y})$:

$$f(\boldsymbol{Y}) = f(y_M|y_{M-1}, y_{M-2,} \dots y_1) f(y_{M-1}|y_{M-2}, y_{M-3,} \dots y_1) \dots f(y_2|y_1) = \prod_{i=1}^{M} f(y_i|\boldsymbol{Y}^{(i)}) \quad (1)$$

where $\boldsymbol{Y}^{(i)} = [y_k : k = 1,2, \dots, i-1]$. The use of (1) would allow to obtain $f(\boldsymbol{Y})$ by recursively computing the conditional distributions $f(y_i|\boldsymbol{Y}^{(i)})$. Nevertheless, the problem still requires a high computational effort, particularly for the estimation of the high-dimensional $\boldsymbol{Y}^{(i)}$ components (i.e., for valuIs of *i* near

to *M*). To tackle this issue, B&A assumes locality and stationarity, which brings to a significant space reduction via subsample selection $\boldsymbol{y}^{(i)} \in \boldsymbol{Y}^{(i)}$ (Efros and Leung 1999; Levina and Bickel 2006). The locality assumption states that the grayscale characteristic of the response pixel can be described by the surrounding pixels, which makes sense in the case we are focusing on.

The stationarity implies that the covariance structure of the intensities observed at two points, is just depending from their distance. This assumption should be also considered realistic for texturing in 3D printing. More in details, the authors suggest considering values of $\boldsymbol{Y}^{(i)}$ in the top-left area around y_i, as depicted in the left panel of Figure *3*.

$f\left(y_i|\boldsymbol{y}^{(i)}\right)$ can be learned using any supervised method, such that $y_i = g\left(\boldsymbol{y}^{(i)}\right) + \varepsilon_i$, where $g\left(\boldsymbol{y}^{(i)}\right)$ is the mean of the conditional distribution $f\left(y_i|\boldsymbol{y}^{(i)}\right)$ and ε_i is is a zero-mean random error that is independent of $\boldsymbol{y}^{(i)}$. The application of a supervised learning method to an in-control image enables the estimation of the conditional mean function $\widehat{g\left(\boldsymbol{y}^{(i)}\right)}$, which provides enough information to detect the deviations from the reference behavior. To this aim, B&A considered adopting a Regression Tree approach (Hastie *et al.*, 2009) to estimate the conditional mean function $\widehat{g\left(\boldsymbol{y}^{(i)}\right)}$, since it requires low training computational effort and can represent general nonlinear relationships. Regression Trees belong to the tree-based algorithms for classification and prediction. This algorithm recursively partitions the predictor space $\boldsymbol{y}^{(i)}$ into successively smaller groups (child nodes) with binary splits, such that the distribution of the response variable in each split is as homogeneous as possible to a given criterion. The search for homogeneous groups is performed at each iteration by means of a greedy algorithm. At each iteration, the predictor space region R, obtained at the previous iteration, is split in two sub-regions, namely $\boldsymbol{R_1}$ and $\boldsymbol{R_2}$, such that an objective function is optimized (for more details, see Hastie *et al.*, 2009). The splitting operation is recursively repeated until a minimum number of elements in each partition is reached, usually, 5. The obtained tree, which has usually a large dimension, is then reduced by pruning.

Given a final partition $\boldsymbol{R} = [\boldsymbol{R}_1, \boldsymbol{R}_2, \dots, \boldsymbol{R}_k, \dots, \boldsymbol{R}_K]$ of the overall space, the estimated value of the grayscale pixel can be expressed as a function of the intensity estimated in the surrounding pixels as:

$$\widehat{y}_i = ave\left(\boldsymbol{y}^{(i)} | \boldsymbol{y}^{(i)} \in \boldsymbol{R}_k\right) \quad (2)$$

In their paper, Buy and Apley use a single reference grayscale image $\boldsymbol{I}_0$ to train the regression tree algorithm, as usually happens in Phase 1 of control charting. Usually, the first layer is printed in stable conditions after the process setup, and it is highly unlikely that the process starts out of control. However, a check should be done (even by visual inspection) before proceeding, in order to avoid a training step under out-of-control conditions. Training could be also performed considering a set of IC images or a virtual IC image obtained by averaging them. This averaging step should further reduce the effect of undetected flawed images on the training dataset.

Some considerations should be added for grayscale prediction of pixels near to the edges and corners of the textured surface image. When pixels are located near to the layer border, the surrounded pixels are partially belonging to the image background. These pixels can be easily filtered out by applying to each image a mask, representing the shape of the current printed layer, whose geometry is known a-priori. The elimination of the background makes the pixels near to the borders surrounded by a lower number of predictors, whose numerosity depends on the window's size. A lower number of predictors can lead to a lower accuracy in grayscale prediction, which can be detrimental for the overall methodology performances. For this reason, we excluded the pixels near to the layer borders from all the algorithm steps.

The fitted model is then employed to perform predictions on pixel grayscale intensity of a new image. Authors underline that if no unusual pattern occurs, then the residuals should behave approximately as white noise. In contrast, if a new image has defects or other departures from the reference stochastic in-control behavior, then the residuals should locally show outliers.

Once the model has been trained with an in-control image, the second step of the algorithm starts, as we can now make predictions on new images and use the residual errors to measure the degree of deviation from the IC model. As stated by B&A, the pairwise comparison between the residuals of the training and testing images could not be sensitive to small mean shifts. For these reasons, authors suggest the

use of a spatial moving statistic (SMS) computed within a square-shaped moving window that is scanned across the residual image. From now on, we will refer to the sliding window size length with *w*.

Given the training residual matrix and its empirical cumulative density function φ, the new residuals $\boldsymbol{r}^{(i)} = \{r_{i,1}, r_{i,2}, \dots, r_{i,n}\}$ observed in the new image in the moving window centered at i surrounded by n pixels are considered to compute the AD statistic:

$$AD_{\boldsymbol{i}} = -n - \sum_{k=1}^{n} \frac{2k-1}{n} ln\{\varphi(r_{i,n})[1 - \varphi(r_{i,n+1-k}]\} \quad (3)$$

where the exponential adjustment of φ can be suggested, following B&A (see B&A for additional details). The resulting values of the $AD_i's$ statistics clearly depend on the residuals observed in the *w*x*w* moving window. Thus, the choice of *w* is a crucial point for defect detection and the size of *w* should be clearly chosen to be larger than the minimum expected defect size. At the same time, *w* should not be too large, as the size of *w* is clearly inducing a significant increase of the computational time. In our case, considering that defects arise at the bead level, a value of *w* equal to the bead width, i.e., 5 pixels, was considered.

The use of moving window and the absence of pixelwise comparison in this algorithm step, as well as for the predictor selection, make this methodology independent of the textured surface shape and, possibly, its geometrical evolution over time. In fact, in the first algorithm step the prediction of grayscale intensity through Random Forest relies on pixels in the moving window. Since this window is usually chosen such that its dimension is way smaller than the entire investigated textured surface, the overall layer shape is not influential on the prediction results. The same can be stated for the second methodology step, i.e., the computation of AD statistics. The window dimensions are usually way smaller than the overall picture size, and the comparison between residuals is perfomed between the distribution of residuals within the window and the residuals distribution of the entire training image. Again, the textured surface shape does not play any role in the computation of the indicator.

Let $AD_{i,j}$ represent the Anderson-Darling statistic computed at pixel *i* of the *j*-th image, these statistics can be eventually used for monitoring and diagnosis purposes. For each image *j*, B&A suggest considering the maximum value of the A-D statistics, named S_j, as monitoring statistic:

$$S_j = max_{i=1\dots M}\, AD_{i,j} \qquad (4)$$

In the paper, B&A build a Phase I control chart by estimating the empirical distribution of S_j and setting the limits in correspondence of the to $\frac{\alpha}{2}$ and 1-$\frac{\alpha}{2}$ quantiles (α = 0.0027).

3.4The proposed approach for 3D printed surface texturing

Starting from the B&A approach, three main novelty elements are proposed in this paper, which are briefly summarized below.

i) The neighborhood windowing for STS modelling. A first minor change to the B&A algorithm, consists of adopting of a more symmetric window around pixel *i* in the first step, where texture modeling is executed. While B&A considered only a portion of the pixel surrounding y_i (left panel of Figure 3) as regressors, we found that including all the neighborhood of y_i within a given window can bring better texture modeling. In fact, 3D printed textures are usually characterized by deposition strategies which occur at different angles with respect to the window driving axis (as in our case, where a 45° or 135° extrusion strategy is considered) and this is why including all the pixels in the neighborhood (and not only the previous ones) can provide a better model learning step.

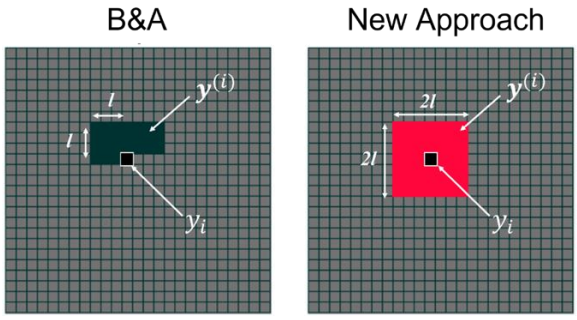

Figure 3 Different windowing strategies. (left) Bui and Apley's approach, (right) proposed apprh.

ii) Random Forest for texture modeling. A second main change proposed in our solution consists of considering a Random Forest instead of a Regression Tree as basic step of the machine learning

algorithm. In our experience, confirmed by the literature, single regression trees can result in high prediction variance. In the case of 3D printed textures, slight changes of the image pattern may cause erroneous predictions, which can detrimentally impact the monitoring performances. Random Forest (together with bagging and boosting) is one of the solutions proposed in the literature to deal with this problem (Hastie et al 2009). It consists of constructing B de-correlated trees and averaging their predictions. The de-correlation among trees is obtained in the tree-growing process by means of a random selection of the input variables. As well as for bagging, each tree is grown from a bootstrapped dataset. Before each tree split, a subset of the input variables is randomly selected as candidate for splitting. Usually, at each iteration, the number of selected variables is set to the square root of the total number of variables. In our case, the construction of the B trees is made using as basic features the intensity of pixels located within a moving window. Then, the predicted value is obtained by averaging the prediction of each tree. Random Forests benefit of performances at least comparable to bagging and boosting, but lower computational time are reported, due to the lower number of variables considered at each step (Hastie et al 2009).

In this application, a Random Forest will be initially trained with an initial image I_0. The trained model will be applied to make prediction on new images. Prediction residuals will be used for monitoring and diagnosis purpose, as described in the A&B approach. In the following case study, the Random Forest will consist of 100 uncorrelated trees. This choice was made as a trade-off between computational costs and prediction performances, as will be shown in a while. Minimum node side was kept equal to 5 pixels, as for the Regression Tree construction.

ii) *K-means clustering for out-of-control detection and localization*. The monitoring solution presented by B&A, which consists of monitoring the maximum of the AD statistic, can lead to high false alarm rates. In fact, the presence of a single pixel with an anomalous grayscale intensity (characterized by a large prediction error) might easily result in an out-of-control point. In common video-imaging applications, the presence of few corrupted pixels is common, and it is usually generated by hardware failures, image compression, environmental disturbances, or acquisition errors (Ji *et al.*, 2010).

One way to increase the algorithm robustness consists of relying on alarm-rules that require a spatially connected zone of outlying pixels to issue an alarm. To this aim, following a similar procedure applied to hot-spot detections in metal-based AM (Colosimo and Grasso, 2018; Bugatti and Colosimo, 2021; Yao et al, 2021) we propose an approach based on clustering for out-of-control detection. Considering the AD statistic assumes large values when a significant difference with respect to the reference distribution of residuals is observed at a given location, the presence of a defect that has a significant extension results in two distinguishable clusters, the first one containing all the non-defective pixels and the second one including the defective ones. In the case of in-control images (where no defects are observed), if the detection of two clusters is anyway forced, both the two clusters will contain small values of the AD's and the largest centroid of the two clusters will take a value quite close to 0 and the value will be anyway used as monitored statistic.

In this application, we adopted the k-means clustering algorithm (Jain et al., 2010) to split all the AD matrixes in two clusters. After the AD matrix is split into two clusters, the cluster centroid with the higher value is chosen as monitoring statistic. Alternatively, other statistics such as the centroids distance or the ratio between the two centroids can be adopted. Based on this statistic, an individual value control chart will be designed (in Phase I using the images collected during Build 1) and used (considering Build 2 in the Phase II of the control chart), considering a Type I error α set to 0.0027.

4. A real case study on Extrusion-based AM

A real case study based on inline images acquired in-situ on AM parts produced via Fused Filament Fabrication (FFF) will be used as reference benchmark throughout this work. It consists of two jobs, namely *Build 1* and *Build 2* made of 99 layers each, where in-situ images obtained layerwise were acquired. A commercial FFF 3D printer (see **Errore. L'origine riferimento non è stata trovata.** for technical specifications) was used with a standard 1,75 mm diameter filament of Polylactic Acid (PLA) printed considering process parameters shown in Table 2.

Table 1 FFF printer -technical specifications (https://www.sharebot.it/en/)

Working Volume	250x220x200 mm
z resolution	0.05 mm
Printing bed calibration system	Integrated
Nozzle diameter	0.4 mm
Max bed temperature	100°C
Max extruder temperature	270 °C

Table 2 – Process parameters used for 3D-printing

Process Parameters	
Extrusion Temperature	220 °C
Bed Temperature	40 °C
Layer height	0.2 mm
Number of contours	2
Infill Percentage	100%
Printing Speed (infill)	80 mm/s
Printing Speed (contours)	65 mm/s
Beads Rotation	90°

Both the printed objects consist of a parallelepiped (20x20x20 mm) using infill set to 100%, to avoid voids inside the printed layer. A standard 90° rotation approach for the deposition strategy was considered, as this strategy is commonly adopted to ensure a better bonding among layers. Thus, the bead orientations were alternatively observed at 45° and 135° on each couple of consecutive layers.

The first layer in Build 1 was used as training image to develop the approach. Then, all the other layers of Build 1 were be used to test the performance when in-control conditions are assumed.

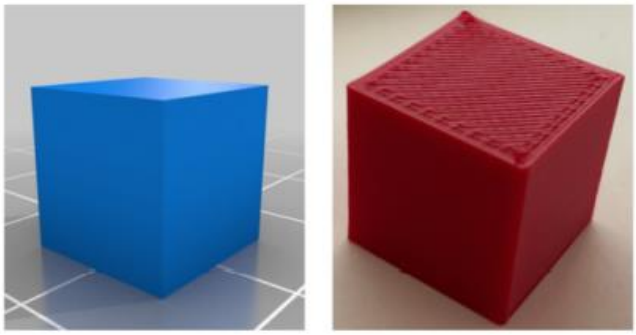

Figure 4 (left) CAD model of Build 1 and Build 2. (right) Picture of Build 1

Build 2 is a replicate of Build 1. The only difference stands in the introduction of artificial defects in some of the printed layers. This was possible by manually modifying the GCODE, by locally changing the infill rate and the filament feed. Two main types of defects were induced, i.e., over- and under-extrusion. The first type of defect was generated by locally increasing the filament feed of about 3 mm on just a portion or the entire rectilinear bead deposited (as shown in Figure 1 b-c). Under-extrusion was instead realized by reducing the infill to 15% on a portion of the bead or the entire bead, as shown in Figure 1 (d). The creation of inter-beads porosity was observed in the layer right after those containing the missing beads. This was due to the lack of material support in the underneath layer, which provoked the bead collapse, which is visible in Figure 1 (f). This type of induced defect will be also considered in this analysis as out-of-control states to be detected.

Layerwise images were acquired with a customized video-imaging system, installed on the top of the printing area. It consists of a iDs ui-5490 camera combined with a Kowa lens with a focal length of 25 mm, mounted on a customized plexiglass support at 200 mm from the top of the build plate (see Figure 5). Camera resolution was set to 10.55 Mpixels (3840 x 2748 pixels), which resulted in a real spatial resolution of around 0.05 mm/pixel. The exposure time was set to 374 ms, to ensure an adequate image brightness. In this case study, the acquisition system was manually activated as a proof of concept for the proposed solution. However, an automated solution that triggers image acquisition upon completion of each layer can be easily implemented. For the acquisition purpose, we modified the GCODE to move the extruder head in the bottom-left corner of the build platform, in order to prevent a partial reduction of the field of view. For each build, 99 images were captured. Each dataset is thus composed of 45 images with bead orientations of 45° and 45 images at 135°. The two image classes show different characteristics in terms of contrast, due to the orientation of the beads with respect to the light source (i.e., the ambient light, mainly coming from the left-hand side of the machine). Example of images with 45° and 135° orientations are reported in Figure 6. The effect of different contrast on the algorithm performances will be deepened in the following sections.

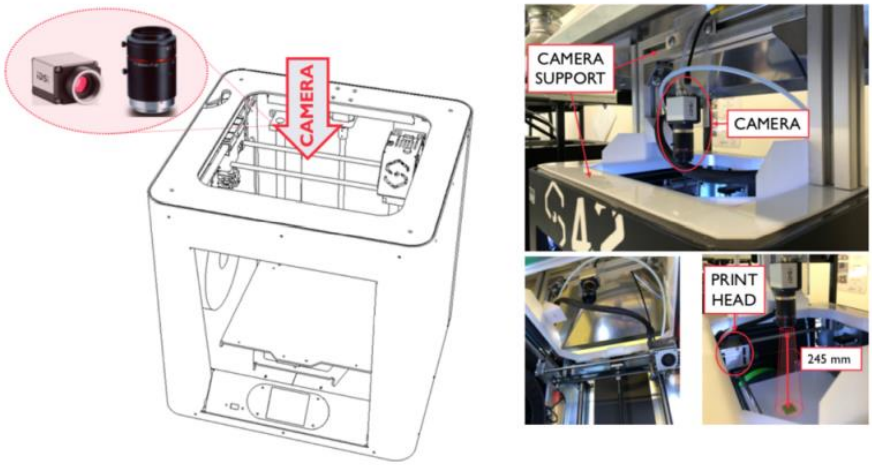

Figure 5 (left) Schematic view of camera position in the 3D printer. (left) Views of the acquisition setup

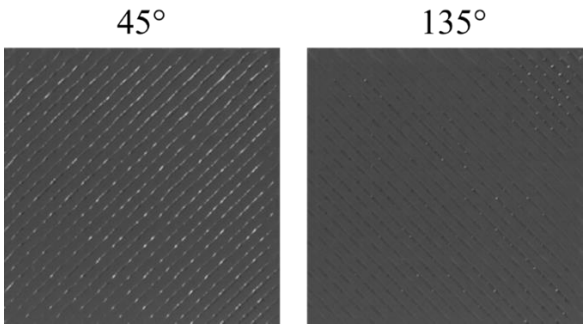

Figure 6 An example of in-situ top layer image with beads oriented at 45° (left) and 135° (right)

4.1 Prediction accuracy

In this sub-section, the effect of different selection of the parameters is compared in terms of prediction accuracy and computational costs. Prediction accuracy is evaluated through k-fold cross validation (Fushiki *et al.*, 2009). More in details, for each fold, three images with bead orientation of 45° and three images with 135° were randomly picked in order to investigate the effect of beads orientation on prediction performances. Thus, a 6-fold cross validation was applied and the 6-fold mean square error (MSE) computed for different window sizes ℓ, to better highlight its influence.

Figure *7* illustrates the results of the MSE computation via 6-fold cross validation for the investigated approaches. The effect of the training image orientation on the prediction performances is highlighted

by different colors, as explained in the legend colormap. 45°- 45° color corresponds to MSE values computed by training a 45° image and testing the resulting model on images with the same orientation. In opposition, 45°- 135° corresponds to the MSE values computed using a 45° image as training image and testing the resulting model on images with the opposite orientation. Similarly, notation 135° -135° and 135° - 45° refer to the training-testing images.

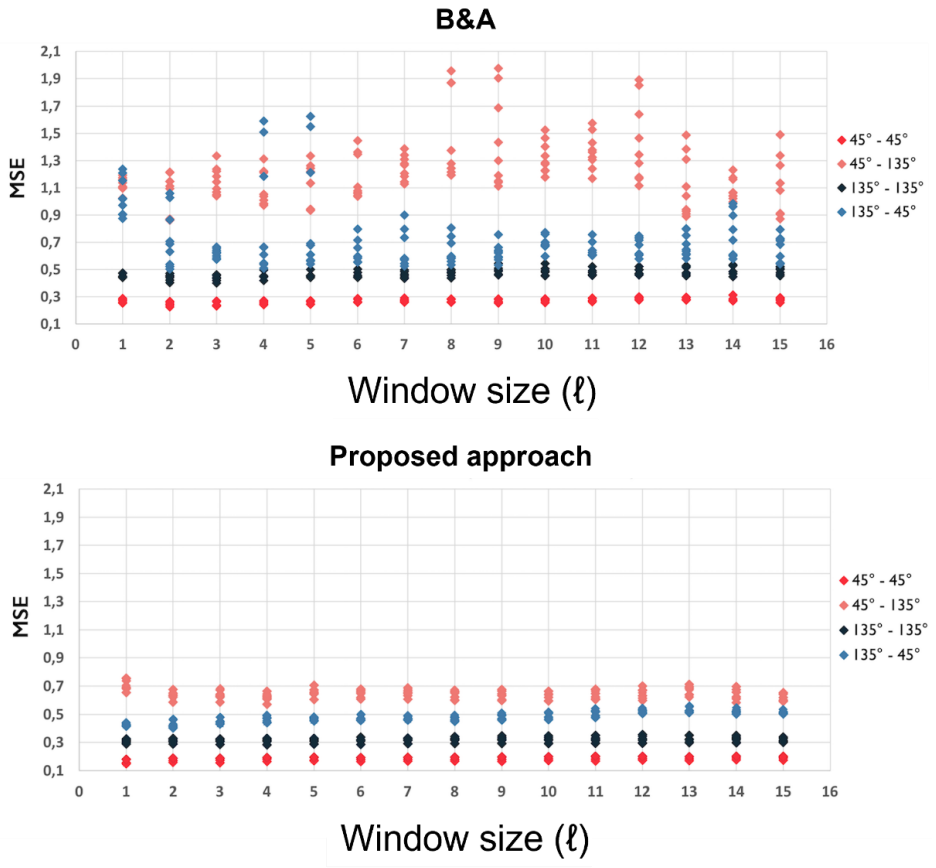

Figure 7 Results of 6-fold cross validation for the approach of Bui and Apley and for the proposed improved methodology. Different points color highlights the relation between the training and test images beads orientation.

Regardless of the window size choice, the application of a Random Forest and the new symmetric windowing approach induce a significant reduction of the average prediction error and the related variance. More in details, an average improvement of around 40% of the prediction accuracy can be observed with our proposed solution. For all the values of ℓ, the MSE remains stable for both the approaches. This finding shows that enlarging the window size does not affect the prediction performance. In other words, most of the information for training the model is simply contained in a

small window of the surrounding pixels. It showes also that, regardless the chosen models, the training and testing image orientations strongly influence the performance results. In general, the same orientation between the training and testing datasets brings to a higher prediction accuracy. Moreover, different performances are observed for 45° and 135° images, due to the different signature of the observed texture, as shown in **Errore. L'origine riferimento non è stata trovata.**. For this reason, from now on, the two image classes will be treated separately.

The effect of the window size is also discussed in terms of computational time, that are calculated by running the algorithm on a workstation equipped with an Intel© CoreTM i7 -2620M @ 2,9 GHz.

Figure 8 shows the training and prediction times for both the investigated methods (B&A versus our proposed solution). The use of multiple trees on the modified approach brings to an evident increase of the training and prediction times. Thus, the higher ℓ, the higher will be the time to train the algorithm and starting the monitoring procedure. This becomes particularly evident for values of ℓ higher than 4.

As regards the prediction times, values of ℓ lower than 8 are compatible with the temporal constraints related to our case study (considering the time required to print a layer).

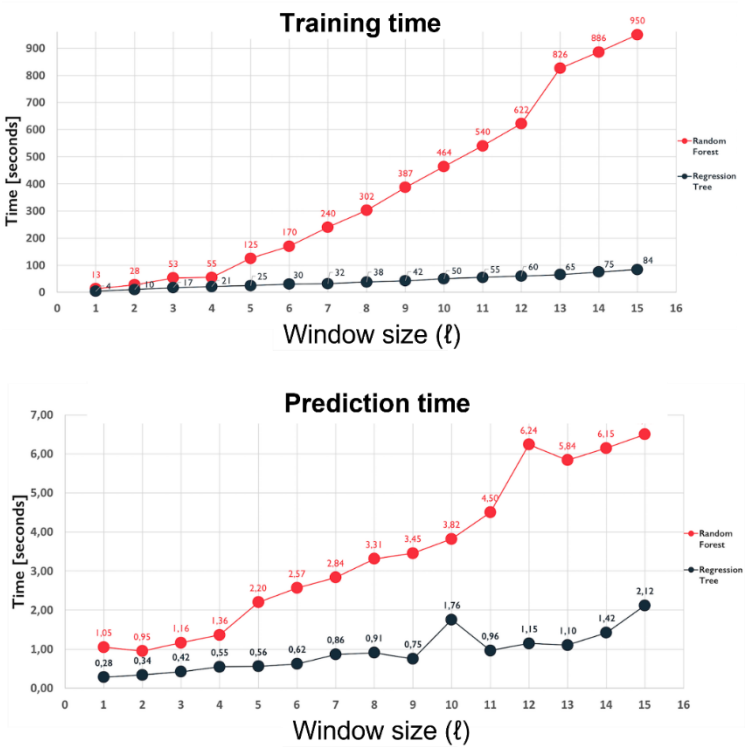

Figure 8 Computational time respectively to train the model (top) and make prediction (bottom) on new images. The two methodologies are distinguished by the lines color.

As the prediction results seem to be almost unaffected by the window size while the computational time is significantly increasing from window sizes larger than ℓ=5, a good compromise is obtained by selecting a window size equal to ℓ=4. Indeed, this window size is comparable with the bead dimension, and it should include enough anomalous pixels values in case of out-of-control occurrence. Moreover, its computational time is suitable for the case study. 135° and 45° images will be treated separately for the computation of the AD statistics and in the control chart construction, due to the different image characteristics and prediction performances.

4.2 Defect detection via AD computation

Figure 9 and Figure 10 show the results of B&A approach and the presented competitor application on examples with orientation of 135° and 45°, taken from the in-control training dataset (Build 1). For both the beads orientation, the application of new windowing strategy and Random Forest bring to an overall reduction of the residual variability. While for the 135° - oriented images, which are characterized by

low contrast, the pattern is filtered through the application of the machine-learning technique, the same cannot be stated for the 45° images, where light spikes in correspondence of the bead edges result in large residual deviation. Nevertheless, the computation of the AD statistic mitigates this effect.

As regards the AD statistics, a higher variability is observed when the B&A approach is applied, meaning that a higher difference between the training and the tested image residuals is observed, even when in-control layers are printed. This can be explained with one of the main limitations of the Regression Tree approach, i.e., the tendency to overfit the data. This problem is notably solved with the Random Forest approach, through the random selection of regressors at each split and the result averaging across different trees. AD statistic for in-control images result to be uniform and close to zero, meaning that a small difference between the training and the testing residuals is observed. The only points with relatively high values of AD arose in the top-right image corner of 135°-oriented images, where inter-bead gaps seldom arose. However, as shown in the following pictures, the values of AD's in correspondence of these small anomalies are way lower than those originated by defects.

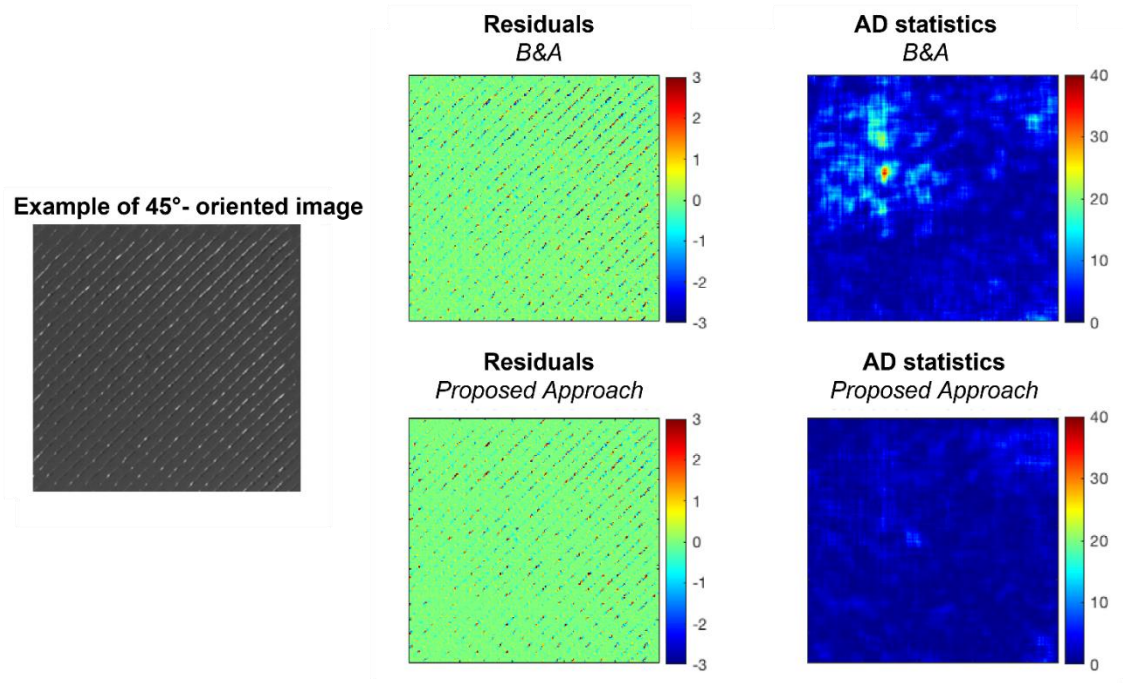

Figure 9 Example of 45° - oriented image. (center) Residuals of the two investigated approaches. (right) AD statistics for the two investigated approaches

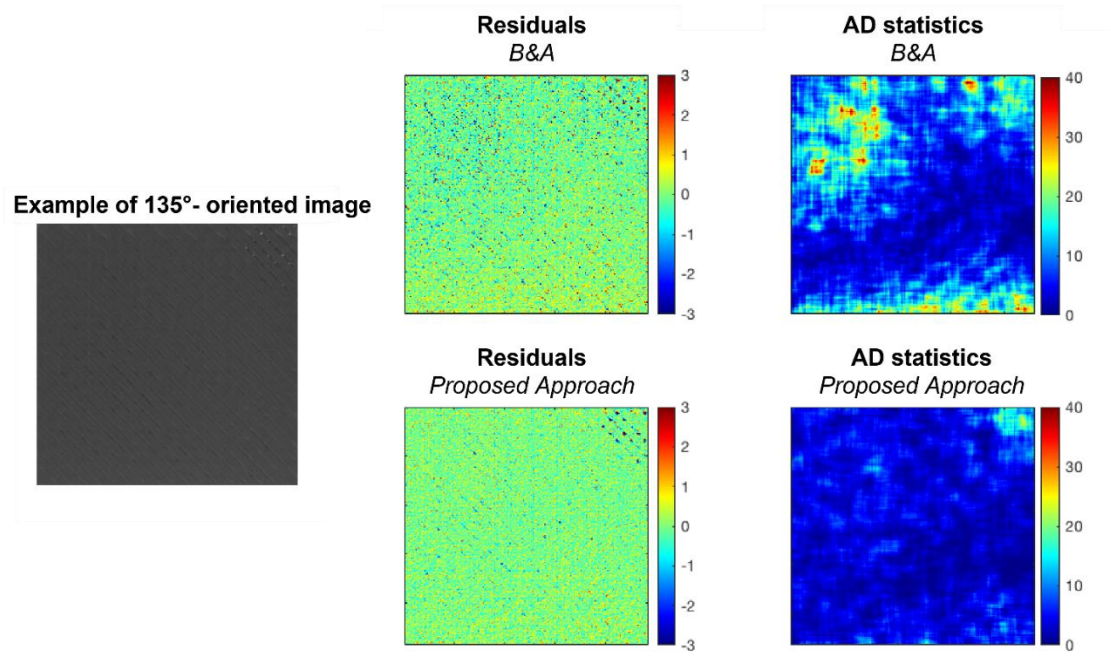

Figure 10 (left) Example of 135° - oriented image. (center) Residuals of the two investigated approaches. (right) AD statistics for the two investigated approaches

The analysis of residuals and AD statistics have been also extended to the OOC images, since their occurrence was controlled. Figure 12 and Figure 11 depict two examples of OOC images for both the beads orientation. Both the approaches put in evidence the presence of local anomalies through high values of the AD statistics, of at least one order of magnitude higher that the areas were no defects are present. Nevertheless, the B&A approach appears again more unstable, showing high values of AD statistics in the areas where no anomalies are present (see for example the top-right panel of Figure *12*). In general, the application of the modified approach generates a higher difference in the AD statistics between the in-control and the out-of-control pixels (as shown in Figure *11*).

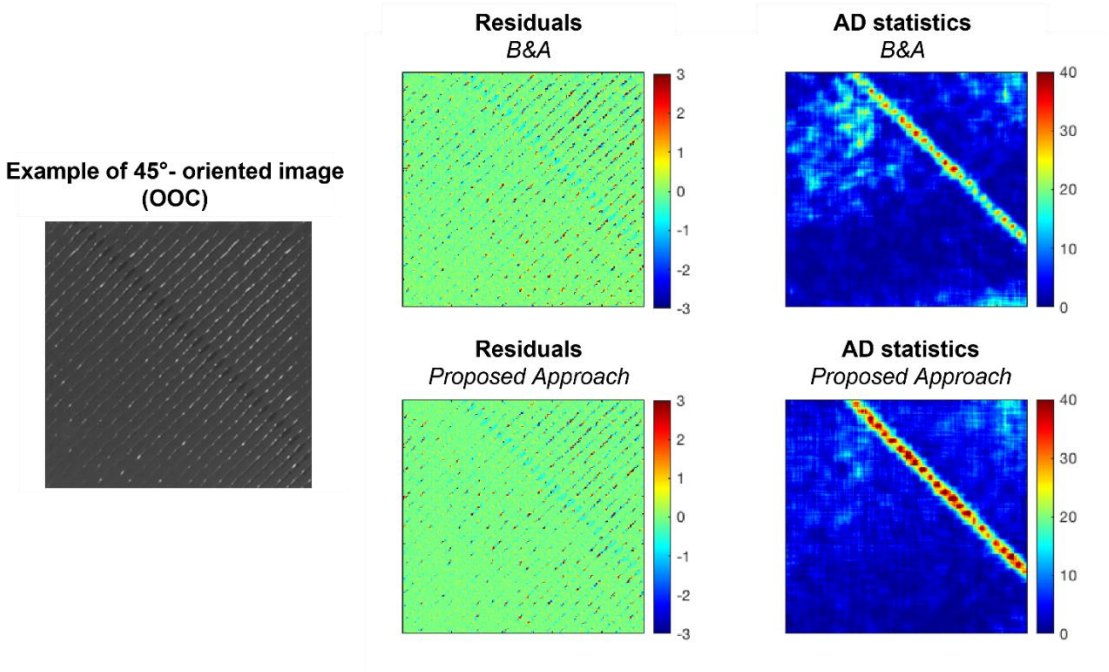

Figure 11 Example of 45° - oriented image containing a deposition defect. (center) Residuals of the two investigated approaches. (right) AD statistics for the two investigated approaches

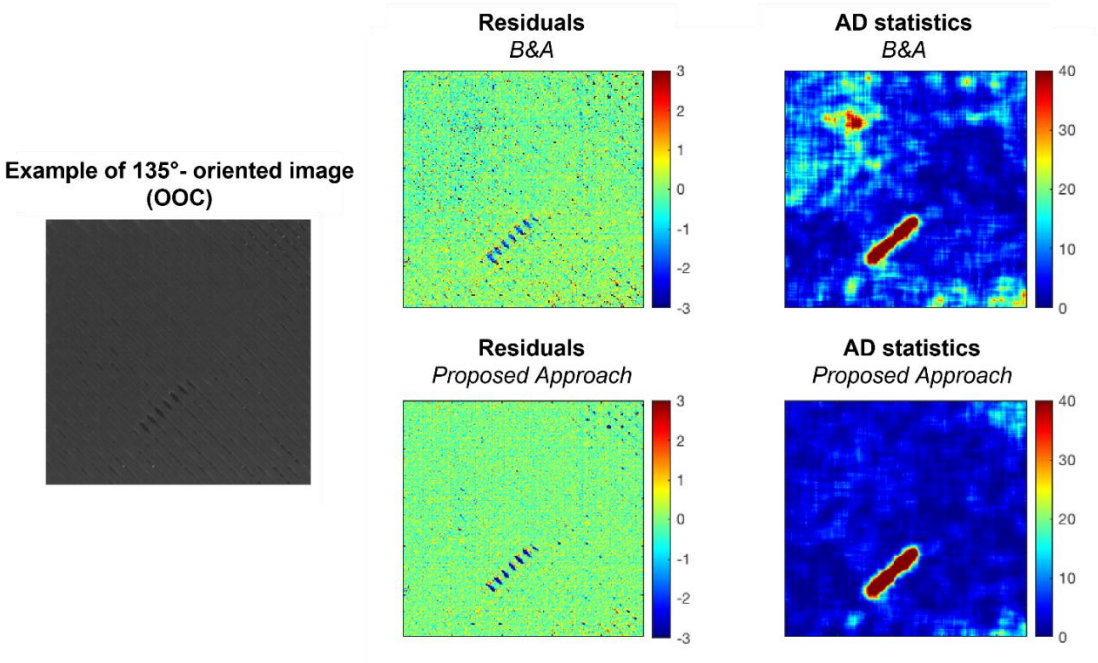

Figure 12 Example of 135° - oriented image containing a deposition defect. (center) Residuals of the two investigated approaches. (right) AD statistics for the two investigated approaches

4.3 Monitoring Results

Figure *13* shows the control charts for both the image orientations and the monitoring algorithms. As regards the B&A monitoring strategy, a first consideration can be drawn looking to the differences between Build 1 and Build 2 in-control values. The maximum AD values of the second build always fall above the center-line value computed during Phase I. Thus, the B&A's monitoring statistic appear to be affected by a build-to-build variability. The mean shift occurs for both the orientations, resulting also in several false alarms for 135° orientation images. All the statistics related to the out-of-control images are above the upper control limit, but this result is mainly generated by the statistic mean shift.

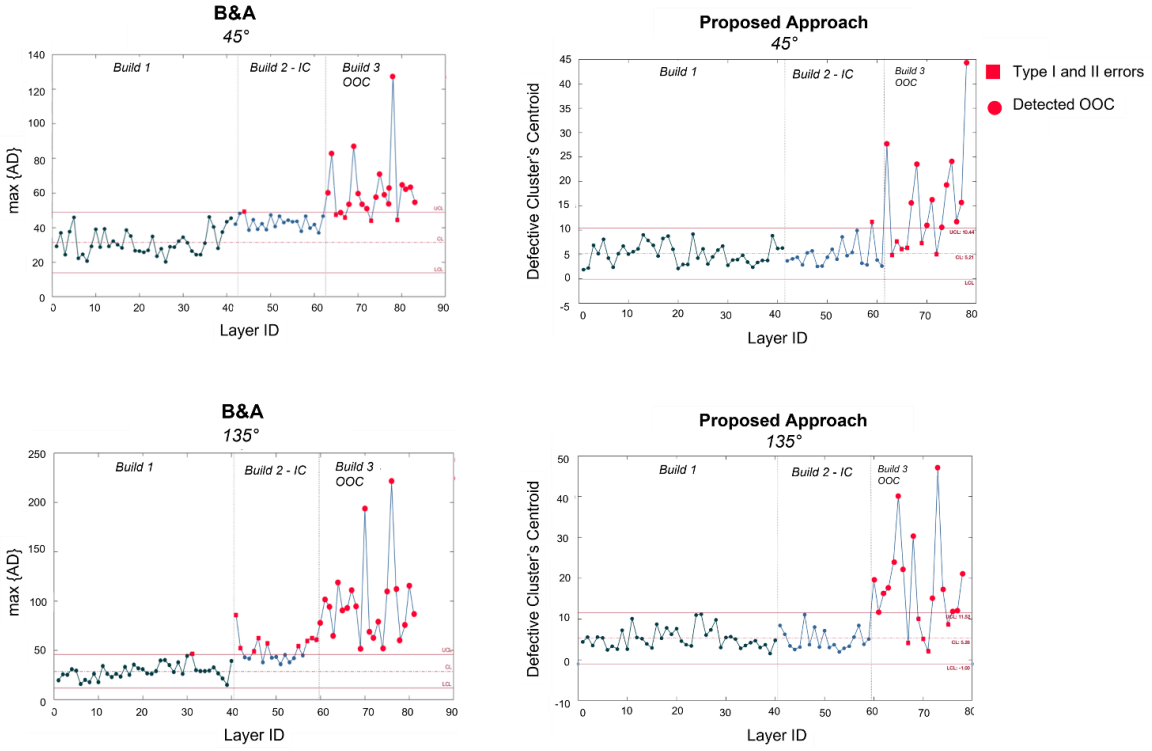

Figure 13 Control charts for 45° and 135° oriented images, obtained through the Bui and Apley approach (left column) and the competitor approach presented in this work (right column).

The build-to-build variability is cancelled out if our newly proposed approach is considered, as our e monitoring statistic appears stable over builds. The application of the improved version of the monitoring methodology brings also to a high number of out-of-control detected, as depicted in the last part of the control chart section. Nevertheless, still some simulated defects are not detected. More in details, 6 over 17 induced out-of-control defects are not detected for the 45°-oriented images, and 5 out

of 18 are undetected for the 135°-oriented images. In general, no evident difference among the control charts related to the 45° or 135° orientations can be noted. The analysis of residuals and AD matrixes of the undetected out of controls highlighted that they do not belong to a specific defect class (neither in terms of defect typology nor in terms of defect size). Two examples of out of controls are reported in Figure *14* and Figure *15*. In both the cases, the k-means clustering, which is used for monitoring and diagnosis purposes, performs poorly due to the low difference between the AD values related to the flaws and the background.

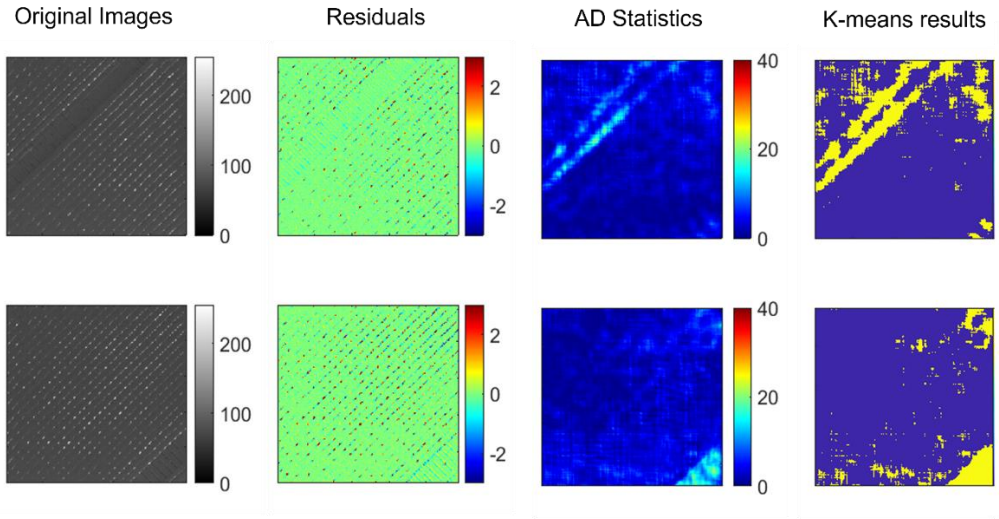

Figure 14 (left) two examples of OOC images for 45° oriented images. Each row shows the original image, the Random Forest prediction errors, the AD statistics and the kmeans (k=2) results.

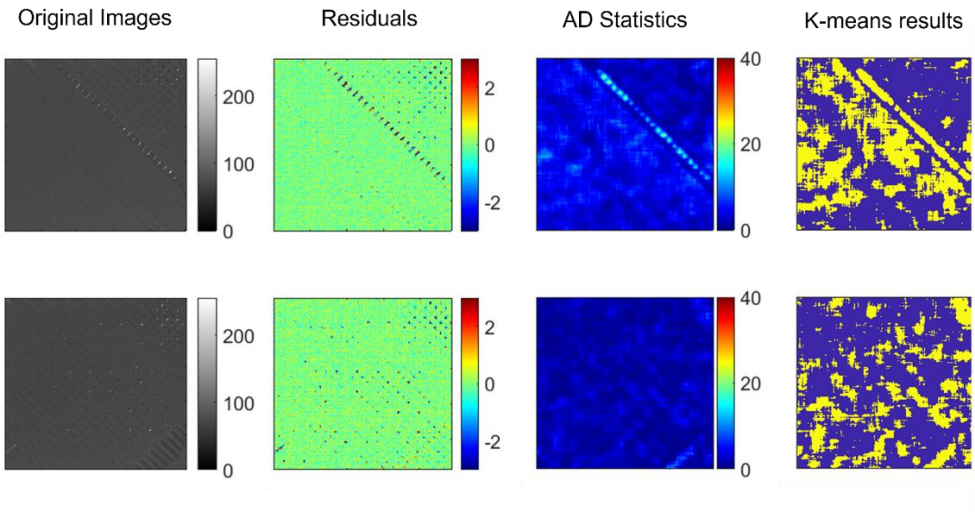

Figure 15 two examples of OOC images for 135° oriented images. Each row shows the original image, the Random Forest prediction errors, the AD statistics and the kmeans (k=2) results.

5. Comparison of the proposed approach with approaches for layerwise surface texture monitoring in extrusion-based AM

The performance of the proposed algorithm is also compared to state-of-the-art methods for layerwise images in extrusion-based AM proposed by Okarma and Fastowicz, who proposed synthetic metrics to detect global deviations from the nominal texture and local texture flaws. Their approaches are based on different metrics: the entropy-based indicator (Fastowicz *et al.*, 2019); four gray-level co-occurrence matrix, namely Homogeneity, Energy, Correlation, and Contrast (Okarma and Fastowicz, 2016); the Feature Similarity Index (SSIM) (Okarma and Fastowicz, 2019), and an indicator based on the Hough transform (Fastowicz and Okarma, 2019). In order to use these metrics in an industrial setting, individual value control charts are built on each of these indexes, assuming a Type I error α set to 0.0027.

Three performance indexes, namely, accuracy, precision, and recall (Hossin and Sulaiman, 2015) are considered to compare the performances of the competing methods. Accuracy measures the percentage of correct predictions, and it is calculated as $\frac{TP+TN}{TP+FP+TN+FN}$, where true positive TP is the number of defective images that are classified as out-of-control, true negative TN are the non-defective images that are classified as in-control, false negative FN are those defective images that are erroneously identified as in-control, and false positive FP is the number of non-defective images classified as out-of-control. Precision (P) measures the portion of correctly classified defective images over all the out-of-controls, and it is defined as $P = \frac{TP}{TP+FP}$. Iall (R) is the percentage of correctly classified defective images, and it is calculated as $R = \frac{TP}{TP+FN}$.

The table below (Table *3*) reported the accuracy, precision, and recall for all the investigated indicators.

Table 3 Accuracy, precision, and recall of all the considered indicators. Results are divided according to the bead orientation.

		Proposed Approach	***Entropy-based***	***Contrast***	***Correlation***	***Energy***	***Homogeneity***	***FSIM***	***Hough-based***
45°	***Accuracy***	81.1%	55.8%	55.8%	55.8%	51.2%	55.8%	60.5%	53.5%
	Precision	91.7%	63.6%	57.9%	80.0%	52.2%	57.1%	64.7%	60.0%
	Recall	64.7%	31.8%	50.0%	18.2%	54.6%	54.6%	50.0%	27.3%

135°	***Accuracy***	86.8%	63.4%	47.6%	45.0%	47.6%	47.6%	45.2%	64.3%
	Precision	100.0%	100.0%	50.0%	44.4%	50.0%	50.0%	33.3%	81.8%
	Recall	73.7%	31.8%	40.9%	19.1%	40.9%	40.9%	4.6%	40.9%

The proposed approach outperforms the competitor indicators for all the performance indexes, regardless of the angle orientation. It shows excellent performance particularly for accuracy and precision, due to the low number of false alarms (only one for 45° orientation) and the correct classification of all the in-control images. Lower results are observed for recall, because of the non-detected defective layers. Also in this case, the new algorithm overcomes the best competitor values of more than 30% for 135° bead orientation images and around 10% for 45° bead orientation.

6. An extension to lattice-textured surfaces

In order to demonstrate the flexibility of our proposed method when patterns different from the one presented in the case study are considered, we applied our approach to layerwise images taken during fabrication of lattice-like structures. These types of shapes are widely adopted in medical, aerospace, and automotive fields when lightweight and resistant structures must be fabricated. Lattice structures are also often used in 3D bioprinting applications as scaffolds, i.e., a temporary structure aimed at promoting the controlled growth of cells in complex shapes.

The image below depicts the results of AD computation for two images of a lattice structure. The first is a non-defective image, while in the second one a defect was artificially simulated by digitally altering the inline image. The introduced defect is meant to simulate an undesired over-extrusion state.

Figure *16* underlines that, also in presence of layer-textured images, the presented method is able to highlight the presence of local flaws through the AD statistic.

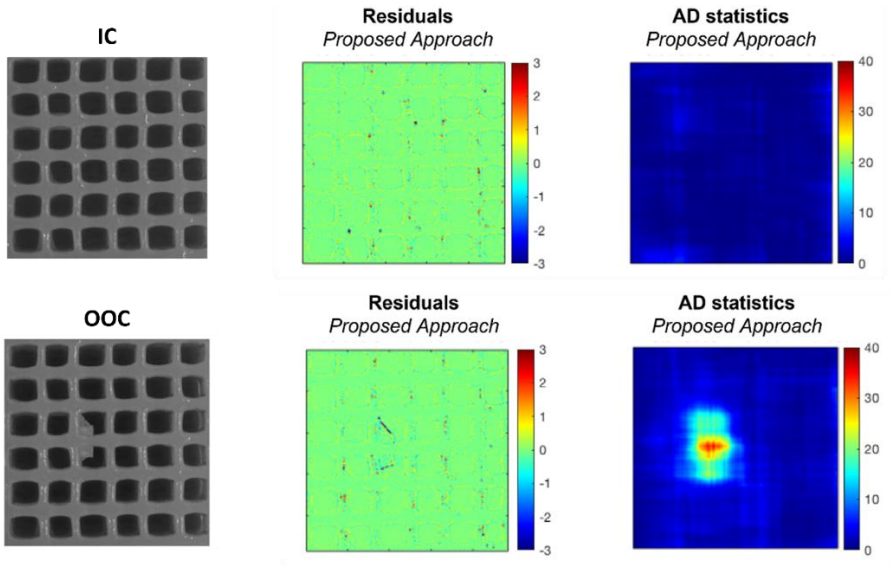

Figure 16 Examples of IC and OOc images for a lattice-like structure. Each rows reports the original image, the residual model and the AD matrix

6. Conclusions

In this work, an approach for statistical quality monitoring of deposition errors in extrusion-based AM via stochastic textured image monitoring was presented. Starting from the seminal paper by B&A (Bui and Apley 2018), we discussed and proposed several novelty elements that made the approach applicable to the case of 3D printing. First, a direction-independent windowing strategy was adopted to include all the pixels surrounding the pixel response. The algorithm to predict pixel grayscale intensity was then changed considering a Random Forest instead of a Regression Tree in order to improve the prediction accuracy. Eventually, a novel solution based on clustering was proposed for the last monitoring stage based on control charting.

Results showed that the proposed algorithm is outperforming the original method, regardless of the window size and the deposition strategy. Moreover, the increase of computational time due to averaging of multiple regression trees in the random forest ensemble is acceptable for AM monitoring purposes. As regards the monitoring stage, the B&A approach appears to be strongly affected by build-to-build variability, preventing its use in real case scenarios. This does not occur to our newly proposed method, which is unsensitive to the build-to-build variability. The comparison with other state-of-the-art

approaches demonstrated that the presented algorithm has a higher ability of identifying images containing local flaws, keeping a low number of false alarms. Finally, the application of the method to layerwise pictures of lattice-like structures highlighted its flexibility towards the change of the images.

Despite these first results, several directions for further research can be considered. Clearly, different case studies can be considered to further test the capability of our proposed solution to different AM processes. The role of other possible modeling solutions for texture description could be considered in the future, as approaches based on smooth sparse decomposition (Yan et al., 2018). Eventually, approaches dealing with texturing monitoring when complex shapes are printed layerwise, can be clearly considered as a direction for future research (Colosimo et al. 2022) while other applications of the proposed solutions to different types of stochastic textured surfaces will possibly highlight further research questions for future work.

Acknowledgments

The present research was partially funded by ACCORDO Quadro ASI-POLIMI "Attività di Ricerca e Innovazione" n. 2018-5-HH.0, collaboration agreement between the Italian Space Agency and Politecnico di Milano.

Data Availability

The data that support the findings of this study are openly available in figshare at https://doi.org/10.6084/m9.figshare.24042891.v1.

References

Alqahtani, M. A., Jeong, M. K., & Elsayed, E. A. (2021). Spatially weighted graph theory-based approach for monitoring faults in 3D topographic surfaces. International Journal of Production Research, 59(21), 6382-6399.

Bertoli, L., Caltanissetta, F., & Colosimo, B. M. (2021). In-situ Quality Monitoring of Extrusion-based Additive Manufacturing via Random Forests and clustering. In *2021 IEEE 17th International Conference on Automation Science and Engineering (CASE)* (pp. 2057-2062). IEEE.

Banadaki, Y., Razaviarab, N., Fekrmandi, H., & Sharifi, S. (2020). Toward enabling a reliable quality monitoring system for additive manufacturing process using deep convolutional neural networks. *arXiv preprint arXiv:2003.08749*.

Bui, A. T., & Apley, D. W. (2018). A monitoring and diagnostic approach for stochastic textured surfaces. *Technometrics*, *60*(1), 1-13.

Bugatti, M., & Colosimo, B. M. (2021). Towards real-time in-situ monitoring of hot-spot defects in L-PBF: a new classification-based method for fast video-imaging data analysis. Journal of Intelligent Manufacturing, 33(1), 293-309.

Caltanissetta F., Grasso M., Petrò S., Colosimo, B. M. (2018). Characterization of In-Situ Measurements Based on Layerwise Imaging In Laser Powder Bed Fusion, Additive Manufacturing , 24, 103-115

Caltanissetta, F., Dreifus, G., Hart, A. J., & Colosimo, B. M. (2022). In-situ monitoring of Material Extrusion processes via thermal videoimaging with application to Big Area Additive Manufacturing (BAAM). Additive Manufacturing, 102995.

Colosimo, B.M., Grossi, E., Caltanissetta, F., & Grasso, M. (2020). Penelope: a novel prototype for in situ defect removal in LPBF. JOM, 72(3), 1332-1339.

Colosimo, B. M., Huang, Q., Dasgupta, T., & Tsung, F. (2018a). Opportunities and challenges of quality engineering for additive manufacturing. *Journal of Quality Technology*, *50*(3), 233-252.

Colosimo, B. M. (2018) Modeling and monitoring methods for spatial and image data. Quality Engineering, 30(1), 94-111.

Colosimo, B. M., Garghetti, F., Pagani, L., & Grasso, M. (2022). A Novel Method for In-process Inspection of Lattice Structures via In-situ Layerwise Imaging. Manufacturing Letters. Volume 32, April 2022, pp 67-72

Colosimo B.M., Grasso M. (2018), Spatially weighted PCA for Monitoring Video Image Data with Application to Additive Manufacturing, Journal of Quality Technology, 50(4), 391-417.

Efros, A. A., & Leung, T. K. (1999, September). Texture synthesis by non-parametric sampling. In *Proceedings of the seventh IEEE international conference on computer vision* (Vol. 2, pp. 1033-1038). IEEE.

Fastowicz, J., Grudziński, M., Tecław, M., & Okarma, K. (2019). Objective 3D printed surface quality assessment based on entropy of depth maps. *Entropy*, *21*(1), 97.

Fastowicz, J., Okarma, K. (2019). Quality assessment of photographed 3 d printed flat surfaces using hough transform and histogram equalization. *J. Univers. Comput. Sci*, *25*(6), 701-717.

Fu, Y., Downey, A., Yuan, L., Pratt, A., & Balogun, Y. (2021). In situ monitoring for fused filament fabrication process: A review. *Additive Manufacturing*, *38*, 101749.

Fushiki, T. (2011). Estimation of prediction error by using K-fold cross-validation. *Statistics and Computing*, *21*(2), 137-146.

Hastie, T., Tibshirani, R., Friedman, J. H., & Friedman, J. H. (2009). *The elements of statistical learning: data mining, inference, and prediction* (Vol. 2, pp. 1-758). New York: springer.

He, K., Zhang, Q., & Hong, Y. (2019). Profile monitoring based quality control method for fused deposition modeling process. *Journal of Intelligent Manufacturing*, *30*(2), 947-958.

Holmes, M. (2019). Additive manufacturing continues composites market growth. *Reinforced Plastics*, *63*(6), 296-301.

Hossin, M., & Sulaiman, M. N. (2015). A review on evaluation metrics for data classification evaluations. International journal of data mining & knowledge management process, 5(2), 1.

Jain, A. K. (2010). Data clustering: 50 years beyond K-means. Pattern recognition letters, 31(8), 651-666.

Ji, H., Liu, C., Shen, Z., & Xu, Y. (2010, June). Robust video denoising using low rank matrix completion. In *2010 IEEE Computer Society Conference on Computer Vision and Pattern Recognition* (pp. 1791-1798). IEEE.

Jin, Z., Zhang, Z., & Gu, G. X. (2019). Autonomous in-situ correction of fused deposition modeling printers using computer vision and deep learning. *Manufacturing Letters*, *22*, 11-15.

Levina, E., & Bickel, P. J. (2006). Texture synthesis and nonparametric resampling of random fields. *The Annals of Statistics*, *34*(4), 1751-1773.

Liu, C., Law, A. C. C., Roberson, D., & Kong, Z. J. (2019). Image analysis-based closed loop quality control for additive manufacturing with fused filament fabrication. *Journal of Manufacturing Systems*, *51*, 75-86.

Narayanan, B. N., Beigh, K., Loughnane, G., & Powar, N. (2019, September). Support vector machine and convolutional neural network based approaches for defect detection in fused filament fabrication. In *Applications of Machine Learning* (Vol. 11139, pp. 283-291). SPIE.

Nuchitprasitchai, S., Roggemann, M. C., & Pearce, J. M. (2017a). Three hundred and sixty degree real-time monitoring of 3-D printing using computer analysis of two camera views. *Journal of Manufacturing and Materials Processing*, *1*(1), 2.

Nuchitprasitchai, S., Roggemann, M., & Pearce, J. M. (2017b). Factors effecting real-time optical monitoring of fused filament 3D printing. *Progress in Additive Manufacturing*, *2*(3), 133-149.

Okarma, K., & Fastowicz, J. (2016). No-reference quality assessment of 3D prints based on the GLCM analysis. In *2016 21st International Conference on Methods and Models in Automation and Robotics (MMAR)* (pp. 788-793). IEEE.

Okarma, K., & Fastowicz, J. (2019). Adaptation of full-reference image quality assessment methods for automatic visual evaluation of the surface quality of 3D prints. *Elektronika ir Elektrotechnika*, *25*(5), 57-62.

Okarma, K., & Fastowicz, J. (2020). Improved quality assessment of colour surfaces for additive manufacturing based on image entropy. *Pattern Analysis and Applications*, *23*(3), 1035-1047.

Oleff, A., Küster, B., Stonis, M., & Overmeyer, L. (2021). Process monitoring for material extrusion additive manufacturing: a state-of-the-art review. *Progress in Additive Manufacturing*, 1-26.

Pagani, L., Grasso, M., Scott, P. J., & Colosimo, B. M. (2020). Automated layerwise detection of geometrical distortions in laser powder bed fusion. Additive Manufacturing, 36, 101435.

Qin, Y., Wen, P., Guo, H., Xia, D., Zheng, Y., Jauer, L., ... & Schleifenbaum, J. H. (2019). Additive manufacturing of biodegradable metals: Current research status and future perspectives. *Acta biomaterialia*, *98*, 3-22.

Straub, J. (2015). Initial work on the characterization of additive manufacturing (3D printing) using software image analysis. *Machines*, *3*(2), 55-71.

Sun, H., Gao, D., Zhao, Z., & Tang, X. (2017). An approach to in-process surface texture condition monitoring. *Robotics and Computer-Integrated Manufacturing*, *48*, 254-262.

Wang, Y., Huang, J., Wang, Y., Feng, S., Peng, T., Yang, H., & Zou, J. (2020). A CNN-based adaptive surface monitoring system for fused deposition modeling. *IEEE/ASME Transactions on Mechatronics*, *25*(5), 2287-2296.

Yan, H., Grasso, M., Paynabar, K., Colosimo, B.M., (2021). Real-time detection of clustered events in video-imaging data with applications to additive manufacturing, IISE Transactions - 021/1/29, p. 1-22

Yan, H., Paynabar, K., & Shi, J. (2018). Real-time monitoring of high-dimensional functional data streams via spatio-temporal smooth sparse decomposition. Technometrics, 60(2), 181-197.

Fabio Caltanissetta received his doctoral degree in Industrial Engineering from Politecnico di Milano (while completing this research work), after completing a MSc in Industrial Engineering at the same university. He is currently Process R&D Specialist at Caracol AM.

Laura Bertoli completed a Master of Science in Industrial Engineering at Politecnico di Milano, Italy (while completing this research work). She is currently Business Data product Specialist at UniCredit.

Bianca Maria Colosimo is Professor in the Department of Mechanical Engineering of Politecnico di Milano. Her research interest is mainly in the area of big data mining for Industry 4.0, with special focus on advanced manufacturing.
She is currently Department Editor of IISE Transactions, Senior Editor of Informs Journal of Data Science, Associate Editor of Progress in Additive Manufacturing and Additive Manufacturing Letters. She has been Editor-in-Chief of the Journal of Quality Technology (2018-2021). She is included among the top 100 Italian woman scientists in STEM.